Development of a new, fully automated system for electron backscatter diffraction (EBSD)-based large volume three-dimensional microstructure mapping using serial sectioning by mechanical polishing, and its application to the analysis of special boundaries in 316L stainless steel

Shao-Pu Tsai, Peter J. Konijnenberg, Ivan Gonzalez, et al.

View Online   Export Citation   CrossMark

ARTICLES YOU MAY BE INTERESTED IN

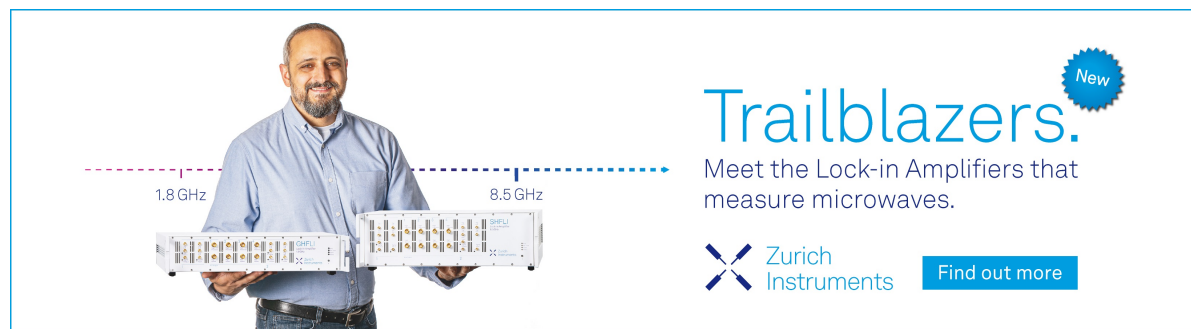Hard x-ray spectrometer calibrations using a portable#120#kV x-ray source
Review of Scientific Instruments **93**, 093529 (2022); https://doi.org/10.1063/5.0099178

Lost alpha Faraday cup foil noise characterization during Joint European Torus plasma post-processing analysis
Review of Scientific Instruments **93**, 093527 (2022); https://doi.org/10.1063/5.0099314

Improved electron trajectory and power distribution in APPLE-knot undulator
Review of Scientific Instruments **93**, 093905 (2022); https://doi.org/10.1063/5.0081034

AIP Publishing

Development of a new, fully automated system for electron backscatter diffraction (EBSD)-based large volume three-dimensional microstructure mapping using serial sectioning by mechanical polishing, and its application to the analysis of special boundaries in 316L stainless steel

View Online Export Citation CrossMark

Shao-Pu Tsai,[1] Peter J. Konijnenberg,[1,a] Ivan Gonzalez,[1] Samuel Hartke,[1] Thomas A. Griffiths,[1,b] Michael Herbig,[1] Kaori Kawano-Miyata,[2] Akira Taniyama,[2] Naoyuki Sano,[2] and Stefan Zaefferer[1,c]

AFFILIATIONS

[1] Max-Planck-Institut für Eisenforschung, Max-Planck-Straße 1, 40237 Düsseldorf, Germany

[2] Research and Development, Nippon Steel Corporation, 1-8 Fuso-Cho, Amagasaki, Hyogo 660-0891 Japan

[a]**Now at:** Forschungszentrum Jülich, IAS-9, 52428 Jülich, Germany.
[b]**Now at:** Department for Lithospheric Research, University of Vienna, Althanstraße 14, A-1090 Vienna, Austria.
[c]**Author to whom correspondence should be addressed:** s.zaefferer@mpie.de. **Tel.:** +49 211 6792 803.

ABSTRACT

We report the development of a fully automatic large-volume 3D electron backscatter diffraction (EBSD) system (ELAVO 3D), consisting of a scanning electron microscope (ZEISS crossbeam XB 1540) with a dedicated sample holder, an adapted polishing automaton (Saphir X-change, QATM), a collaborative robotic arm (Universal Robots UR5), and several in-house built devices. The whole system is orchestrated by an in-house designed software, which is also able to track the process and report errors. Except for the case of error, the system runs without any user interference. For the measurement of removal thickness, the samples are featured with markers put on the perpendicular lateral surface, cut by plasma focused ion beam (PFIB) milling. The individual effects of both 1 μm diamond suspension and oxide polishing suspension polishing were studied in detail. Coherent twin grain boundaries (GBs) were used as an internal standard to check the removal rates measured by the side markers. The two methods for Z-spacing measurements disagreed by about 10%, and the inaccurate calibration of the PFIB system was found to be the most probable reason for this discrepancy. The angular accuracy of the system was determined to be ~2.5°, which can be significantly improved with more accurate Z-spacing measurements. When reconstructed grain boundary meshes are sufficiently smoothed, an angular resolution of ±4° is achieved. In a 3D EBSD dataset of a size of 587 × 476 × 72 μm^3, we focused on the investigation of coincidence site lattice $\sum 9$ GBs. While bearing predominantly a pure tilt character, $\sum 9$ GBs can be categorized into three groups based on correlative 3D morphologies and crystallography.

I. INTRODUCTION

Understanding materials' properties based on their microstructures is one of the key tasks of materials science. The term microstructure refers to the totality of extended defects of crystalline materials, in terms of their kind, density, and spatial distribution. Extended defects are, for example, grain and phase boundaries, dislocations, precipitations, voids, and elastic and plastic strain fields. Although microstructure characterization by microscopy

techniques often results in two-dimensional images, microstructures are three-dimensional (3D) and the three-dimensionality certainly influences all properties of materials. The corrosion resistance of stainless steels, for example, depends on the 3D characteristics of grain boundaries; the efficiency of polycrystalline solar cells is influenced by the 3D arrangement of grain boundaries, and the strain hardening behavior of aluminum alloys is affected by the 3D arrangement of dislocations and the shape and distribution of precipitations.

Several 3D characterization techniques, from (sub-)nanometers to millimeters, thus appear to promote the understanding of microstructure—property relations. In general, all the methods can be broadly grouped into non-destructive and destructive techniques. For the non-destructive techniques, ultrasound tomography[1,2] and x-ray (micro-)computed tomography (CT)[3–5] are two well-known techniques. For the latter, radiation from synchrotron (parallel, high flux) or lab-based (divergent, lower flux) x-ray sources passes through a specimen, and the projections of either the attenuation of intensity, phase contrast, or diffraction signals are collected and computationally reconstructed into a tomogram.[3–6] Recently, lab-based x-ray sources and detectors give a resolution comparable to synchrotron devices, but sub-micrometer spatial resolution is still hardly achievable without a compromise with respect to acquisition time and sample size for a sufficient peak-to-background ratio.[3] The major advantage of non-destructive methods over the destructive ones, described here below, is that they are able to provide very valuable *in situ* observations during e.g., mechanical testing or thermal treatments.

Among the destructive methods, transmission electron microscopy (TEM) tomography[7,8] and atom probe tomography (APT)[9,10] provide structural and/or chemical details down to (sub-)nanometer resolution. In contrast, to acquire materials' information from larger scale, serial sectioning must be resorted to. Till date, several distinct methods have been developed, all based on conducting repetitive serial sectioning either by dimpling,[11,12] machining,[13–15] ablation using ion or photon sources,[16–21] or grinding/polishing.[22–33] After each sectioning, the exposed surface is imaged either by light optical-[11–15,22–31] or electron-microscopy;[16–21,32,33] electron backscatter diffraction (EBSD) and energy dispersive x-ray spectroscopy (EDS) detectors could be optionally outfitted to the latter case.

Machining, also known as micro-milling, can only cope with soft materials, e.g., Pb–Sn alloy, soft Al, or bio-materials, in order to make scratch-free cross sections. In contrast, Ga^+-focused ion beam (FIB) milling is more widely used for accurate and plane-parallel removal of material from a surface.[16–18] However, the totally removed volumes are small: given a maximum size of the removable surface area about $50^2 \ \mu m^2$ and a maximum depth of 50 μm, only a few grains can be observed in the microstructure with a grain size in a tens of micrometer range. Therefore, researchers proposed other types of radiation to replace the Ga^+ beam, such as a focused Xe^+ plasma beam,[19] a broad Ar^+ ion radiation,[20] and femtosecond laser.[21] Sometimes even combinations of different radiations were used for coarse and fine milling. A comparison of the different sectioning methods has been presented in a recently published overview article.[34]

Besides the above-mentioned endeavors to bridge the gap between the probed volume and spatial resolution,[19–21] large-area serial polishing combined with multi-modal observations (i.e., EBSD and EDS) in scanning electron microscope (SEM) is also regarded as a potential candidate, since normal metallographic polishing techniques are well-suited to prepare samples with fields of view up to millimeters or even centimeters in diameter.

The usage of serial sectioning through grinding/polishing dates back to the early- and mid-1900s when pearlite structures were analyzed.[25,26] It is interesting to note that not until recently was Hillert's original work on pearlite[26] being properly reconstructed,[31,35] indicating a lack of suitable tools that could be used to interrogate large datasets in early times.

In 1976, Rhines *et al.*[27,28] employed grinding and polishing to study the topological parameters of Al; the same method was adopted later by Hull *et al.*[29] in 1990 to study the morphology of prior beta grain boundaries of Ti. With the advancement of computer software, Mangan *et al.* revealed the Widmanstätten cementite in 12.3 wt. %-Mn steels,[30] while Kral *et al.* resolved the microstructures of proeutectoid cementite, proeutectoid ferrite, and pearlite, respectively, in 3D.[31] Besides 3D stacks of optical micrographs, Rowenhorst *et al.*[32] were among the first who integrated EBSD, investigating the 3D crystallography of coarse auto-tempered martensite. A similar method was applied by Spanos *et al.*[33] in combination with finite element modeling on β-Ti. It is noteworthy that, due to unintegrated systems and low scan rates of EBSD, in studies Refs. 32 and 33, EBSD scans were still performed manually and not on every section (e.g., on every tenth slice basis in Ref. 33).

Since huge amount of labor and time need to be invested in manual serial polishing,[22,36] automation of the whole polishing and imaging processes is desired. As pioneers, the prototypical Robo-Met.3D[37] and LEROY[38,39] systems built by U.S. Air Force Research Laboratory, the robotic serial sectioning system (RS3D) developed by U.S. Naval Research Laboratory,[40,41] and the Genus_3D™ system reported by Adachi *et al.*[24] have been set up. Among them, LEROY and RS3D are able to perform multi-modal analyses, with a recent study showcasing the capability by analyzing additively manufactured 316L stainless steel.[41]

Inspired by the previously mentioned pioneering works, in the present paper, first, we would like to give a general introduction to our recently completed automatic **E**BSD-based **la**rge-**vo**lume **3D** system, ELAVO 3D. Then, from a complementary viewpoint to the previous literature, we aim at systematically addressing details like how we designed polishing recipes, what are the effects of using different polishing conditions and clean media, how we made reliable sample transfer, etc. Abundant coherent twin [coincidence site lattice (CSL) Σ3] grain boundaries (GBs) in a fully recrystallized 316L stainless steel were chosen as an internal standard to evaluate the reconstruction results. Finally, special attention is paid to the formation mechanisms of CSL Σ9 GBs, which are the product of two meeting Σ3 GBs.

The prime interest of all the above-mentioned 3D-microstructure observation systems is to reach a length scale and resolution of investigation that allows us to make a connection between macroscopic properties and microscopic features for many engineering and geo materials. The resolution of EBSD ranges between 50 nm (e.g., for materials with atomic number, Z > 25) and 500 nm (for Z < 14) (see, for example, the discussion by Tripathi and Zaefferer[42]). These values thus set the lower bound for potential

investigations. It appears that a map area of 1000 × 1000 pixels is usually a size that can be handled well. If such a map is measured with the smallest reasonable 3D step size, provided the correct slice thickness can be reached, a maximum material block size of 50^3 to 500^3 μm^3 would result. Many engineering and geo-materials have grain sizes in the order of 10–100 μm. A map of 50^3 μm^3, which is the largest size that can be delivered by Ga⁺-FIB-milling, would thus just cover between less than 1 to about 100 grains. This is in most cases too little to obtain statistically relevant datasets of grain boundaries, for example. On the other hand, in a 500^3 μm^3 volume, which can be produced by the system introduced here, ELAVO 3D, there would be between 100 and 100 000 grains, which appears much more reasonable. We refer to this volume as "large". Likewise, for a material with 1 μm grain size already a volume of 50^3 μm^3 may be called "large."

To pinpoint ELAVO 3D, Fig. 1 displays resolution and maximum volume diameter of various 3D techniques that are able to reveal microstructural information of crystalline materials. The graph, at the same time, displays typical microstructural features that are investigated with these techniques.

II. SYSTEM DESIGN

The whole automated 3D system is shown in Fig. 2. It consists of three major components: (i) a polishing automaton (Saphir X-Change, QATM), which removes layers of approximately constant thickness from the sample surface by mechanical and chemo-mechanical polishing; (ii) a collaborative robot (UR 5, Universal Robots), which transfers the sample between the polishing automaton and the microscope; (iii) a scanning electron microscope (crossbeam 1540 XB, ZEISS) equipped with electron backscatter diffraction (EBSD), energy dispersive x-ray spectroscopy (EDS), backscattered electron (BSE), and secondary electron (SE)
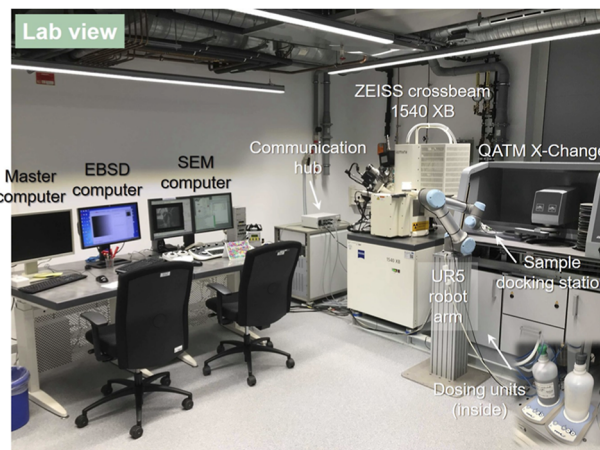

FIG. 2. Overview of the automated 3D system; all individual devices are labeled.

detectors for observation of the serial sections. In-house built software installed on the master computer receives/sends input/output (I/O) signals from/to a communication hub and the servers of the SEM and the EBSD (EDAX) computers, controlling the whole process. The communication hub is responsible for receiving/sending I/Os from/to four parts: the polishing automaton, the robot arm, a stepper motor responsible for releasing and fixing the sample in the polishing automaton, and a z-position sensor. The motor and the sensor are installed underneath a sample transfer bay. The system is designed to run cycles of polishing-based serial sectioning and subsequent SEM observation of these sections without human intervention, with the software being able to track the process of sample preparation and data acquisition and sending error messages, if any, to users via email notification.
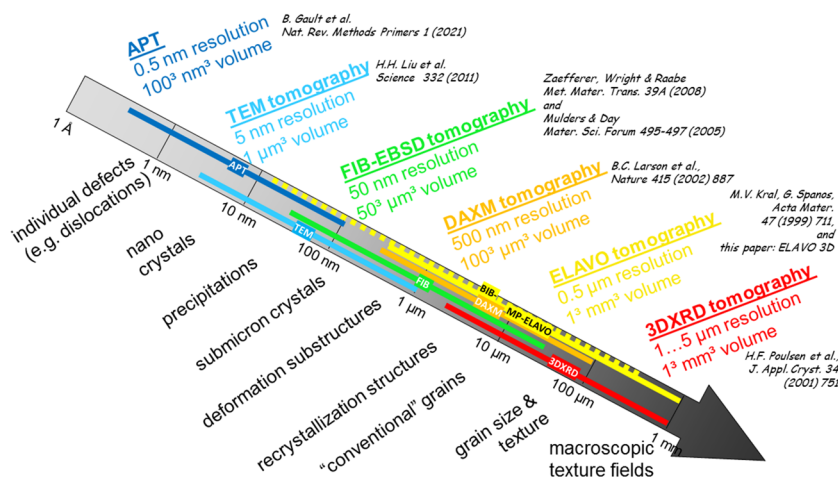

FIG. 1. Overview on resolution, maximum observable volume, and potential applications in materials of different 3D techniques applicable to study crystalline materials. The yellow solid bar of the large-volume systems (ELAVO, in general) corresponds to the technique described in this paper and its competitors, PFIB and laser-FIB. The broken yellow bar corresponds to the broad ion beam system, discussed briefly in Sec. VI B. APT: atom probe tomography; TEM: transmission electron microscopy; FIB: focused ion beam; EBSD: electron backscatter diffraction; DAXM: differential aperture x-ray microscopy; ELAVO: EBSD-based large-volume 3D system, this covers MP: mechanical polishing, PFIB: plasma-FIB, LASER FIB and BIB: broad ion beam; and 3D XRD: three-dimensional x-ray diffraction.

The commercially available QATM Saphir X-Change polishing automaton is used to remove a layer of predefined thickness from the sample by grinding and polishing. Furthermore, the sample is cleaned and dried to achieve a flat and clean surface, ready for SEM observation. By standard, the machine is equipped with up to 16 different grinding/polishing/cleaning cloths and can dose up to four different diamond suspensions, one oxide polishing suspension (OPS) solution, and one cleaning medium (typically ethanol). Furthermore, it includes a cleaning bath that employs ethanol, water, and compressed air. For our aims, the machine was significantly modified in two respects. First, the original ultrasonic bath was replaced by a sample transfer bay from where the specimen is transferred to and from the microscope. Moreover, the polishing head was equipped with a rotation sensor such that the sample can be reproducibly positioned on the sample transfer bay. This station, shown in Fig. 3, is a particularly important part of the system. The sample is placed in a tightly machined recess as the ones visible on the left and the top of Fig. 3(a). An Allen key, visible next to the sample in Fig. 3(a), is responsible for fixing/releasing the sample onto/from the sample carrier. It is operated by a stepper motor below the sample transfer bay. Important parts of the transfer bay are furthermore a guidance pin and a z-position sensor, both of which allow a safe and exact landing of the sample carrier onto the transfer bay. The landed sample carrier is displayed in Fig. 3(b). In order to keep a flat and balanced position during the polishing, the sample carrier contains two additional balance samples that continue to be fixed in the plate. Finally, note that two magnetic stirrers were installed in the cabinet of the polishing automaton (displayed in the bottom right corner of Fig. 2) to prevent possible sedimentation of the used polishing suspension.

A Universal Robot UR5 collaborative robot arm (equipped with a Weiss Robotics WSG25 gripper) is programmed to smoothly transfer the sample between the sample transfer bay and the holder inside the SEM. UR5 features a sample transfer repeatability of ±0.1 mm. Six joints, including base, shoulder, elbow, and three wrists, provide six degrees of freedom, enabling the reachability of the robot arm to any 3D position within its moving sphere. The gripper at the robot arm is equipped with two in-house designed fingers of which one is designed to have a flat edge, fitting a flat counterpart on the sample, in order to minimize the rotation. It provides a rotational precision of ±0.5°.

III. DESIGN OF POLISHING RECIPES

The QATM polishing automaton allows accurate control of all polishing parameters, including pressure of the polishing head, rotational speed/sense of the polishing platen/head, and the amount of abrasive applied per time interval. Nevertheless, it is challenging to obtain constant removal rates, the main reason being the unclear roles of two principle polishing steps [i.e., diamond suspension and oxide polishing suspension (OPS)].

In Sec. III A, we will first explain how the removal rate is measured, with the following two sections focusing on designing reliable polishing recipes using 1 μm diamond suspension and OPS. Finally, the procedures required for sample cleaning will be described. The benchmark sample used throughout the present study is the same 316L stainless steel as the one reported in Ref. 43.

A. Thickness measurements

In order to achieve a stable removal rate, an accurate method for measurement of material removal is necessary. As opposed to other approaches using indentations,[11,12,22,30,32,41,44] autofocus height difference,[23] or laser interferometry,[23] we developed a method based on patterns applied to the side surfaces of the specimen.[45] A plasma focused ion beam (PFIB) was employed to cut M-shaped patterns onto the polished faces perpendicular to the surface of interest. Similar methods can be found in Refs. 20 and 33, with the advantage of this methodology explained in Ref. 33. We used an ion beam current of 2 nA, a voltage of 30 kV, and a 50% beam overlap. After the application of the markers, the sample was electroplated with Ni that reliably filled the channels caused by the milling and thus avoided the formation of pores that might collect dirt during the polishing. Finally, the sample was hot mounted in electrically conductive resin and manually ground and polished until a flat and nearly defect-free sample surface was achieved.

Figure 4(a) sketches where the PFIB markers were applied to the sample. The angles between the inclined and the perpendicular lines are exactly 45° so that the difference in marker distances [$\Delta d1$ and $\Delta d2$ in Fig. 4(b)] can be directly interpreted as removed thickness. Two perpendicular parallel lines of the left and right sides of the markers serve as stationary position markers and are used for magnification calibration. Two sets, i.e., "front face" and "side face," of markers were used to assess the planarity and parallelism of the sample during polishing, the results of which will be shown in Sec. III B. The averaged removal thickness is then defined as the average value of $\Delta d1$ and $\Delta d2$. Figure 4(b) shows the markers observed from the cross section, and Fig. 4(c) displays the markers on 16 consecutive slices where the averaged removal rate was measured as ~1 μm/slice. All removal measurements
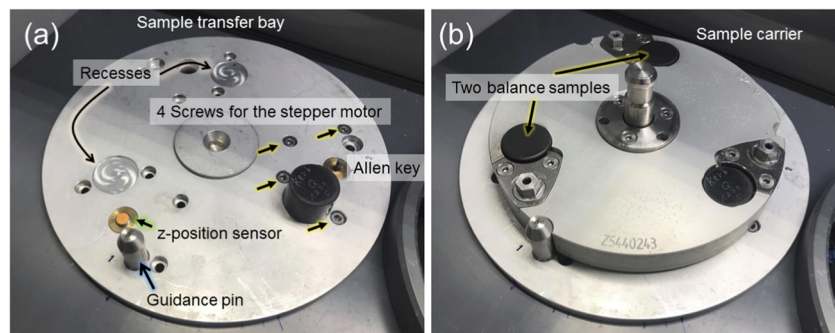
FIG. 3. Closer look at the sample transfer bay in the QATM polishing automaton. (a) The Allen key is used to fasten/release the sample powered by a step motor installed under the plate. The guidance pin and the z-position sensor are used to assure successful landing. (b) Transfer bay with successful landed polishing plate.
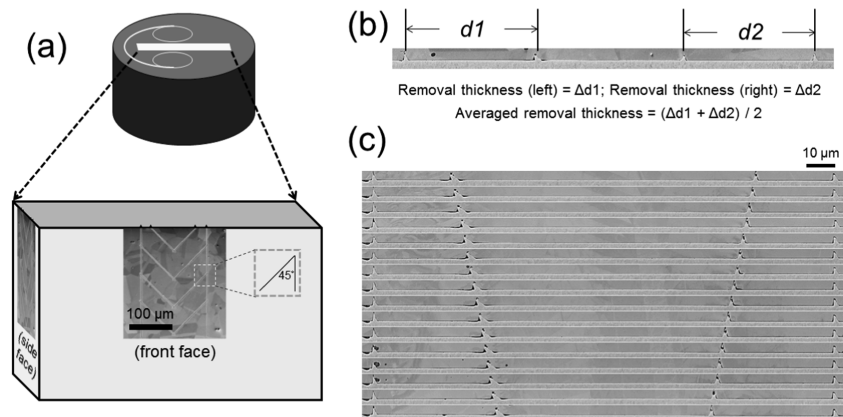
FIG. 4. The method for measuring the removal rate. (a) shows the layout of the mounted samples with PFIB patterns on both the front face and the side face of the sample. (b) defines how to calculate the removal rates, while (c) demonstrates 16 consecutive layers of markers with an average removal rate being 1 μm/slice.

were done using the fully automated 3D system; the SE images were taken under a magnification of 300 with a resolution of ~100 nm/pixel.

B. Mechanical polishing and its effect on the removal rate

Water-based polycrystalline 1 μm diamond suspension provided by QATM was used as main abrasive to remove the desired thickness of material. In this step, the dosing amount of diamond suspension and lubrication, the exerted force and the rotation speed of the head and the polishing platen, as well as the time applied for polishing all need to be well controlled to maintain a reliably stable removal rate. As there are simply too many parameters that may alter the removal rate, the following parameters were set constant throughout the study: The rotation speed of the polishing platen: 155 rpm; the rotation speed of the sample carrier: 145 rpm; and the dosing amount of lubricant: 0.5 ml of dosing every 30 s.

The diamond polishing cloth was not cleaned in between the successive polishing sessions. The effect of the amount of dosing of the 1 μm diamond suspension, the polishing time, and the force were then systematically investigated, and the results are shown in Figs. 5 and 6.

Figure 5 shows the effect of varying the amount of dosing of 1 μm diamond suspension. Throughout the slices, the polishing force was kept at 80 N, and the time used for polishing was set to 2 min. In a first experiment, a larger (though undefined) amount of diamond was applied once to the polishing cloth. The dosing was then switched off completely, and the evolution of removal rates was observed over the next 30 slices. Figure 5(a) shows that the removal rate dropped from 2.25 μm/slice to less than 1 μm/slice over the first 20 slices. From slice 21 to slice 30, the removal rate became more stable, but a decreasing trend is still clear. Note that, in the same figure, the measurements of removal rate using the left side and the right side of the markers are very close to each other, indicating plane-parallel removal.
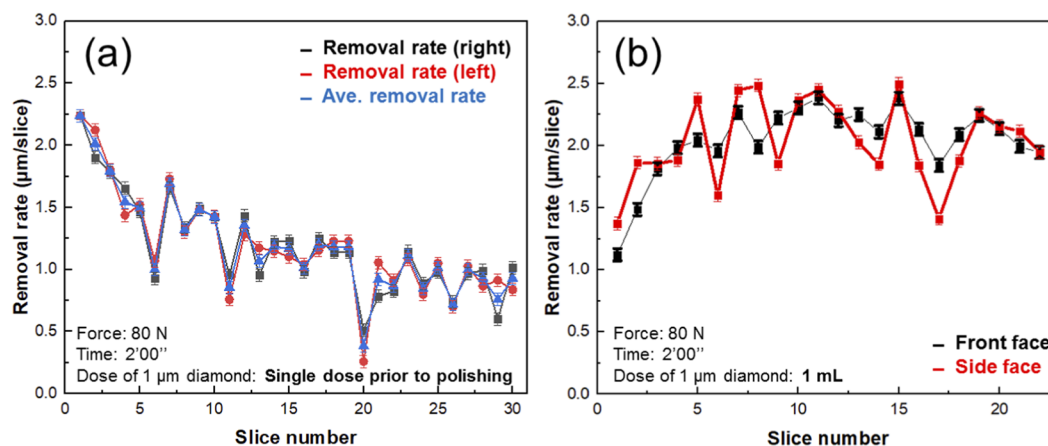

FIG. 5. Effect of dosing of 1 μm diamond slurry. (a) Removal rates determined from the "front face" markers after switching off dosing 1 μm diamond slurry. Black, red, and blue stand for values determined from the right, left, and the averaged value from the PFIB marker. (b) Averaged removal rates measured from the "front face" and "side face" PFIB markers after starting dosing 1 μm diamond slurry. The exerted force, the time used for polishing, and the dosing amount of 1 μm diamond slurry are shown in the bottom-left corner of each plot.
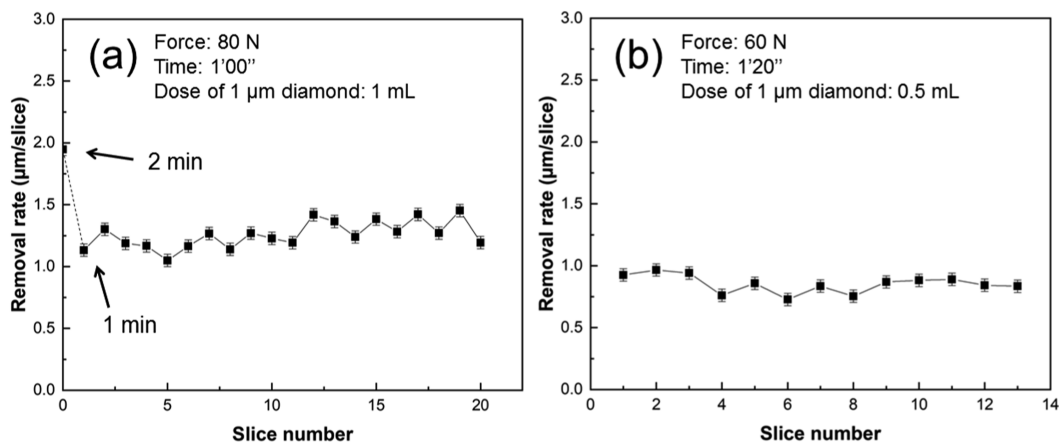
FIG. 6. (a) Effect of polishing time using 1 μm diamond slurry. The dashed line indicates a change of polishing time from 2 to 1 min. (b) Situation with steady state removal rate (~0.85 μm) reached by optimizing altogether the force, time, and the amount of dosing. The exerted force, the polishing time, and the amount of dosing are shown in the upper-left corner of each plot.

In the next step, dosing of 1 μm diamond suspension was activated again with a dosing of 1 ml for the total polishing time of 2 min. Figure 5(b) shows that within eight slices the removal rate increased from ~1.3 to ~2.1 μm/slice, reaching approximately the same level as the one at the starting point of Fig. 5(a) and then staying approx. constant. Note that, in this figure, measurements of removal rate from both the "front face" and the "side face" markers [as indicated in Fig. 4(a)] are presented. Although for each individual measurement, the "front face" and the "side face" show relatively large variations in removal rates, the averages of all 22 measured removal rates are only different by 0.2%, which again indicates that the sample remains plane parallel. Therefore, the removal rate hereafter will only be presented from the "front face" marker results.

Figure 6(a) shows the effect of reducing the polishing time from 2 to 1 min. The removal rate drops from about ~2 to ~1.1 μm/slice, agreeing quite well with the time drop ratio. However, the removal rate shows an increasing trend on continuing polishing. After 20 slices, the rate had climbed to ~1.3–1.4 μm/slice. The reason for this is that the suspension dosing amount (1 ml) was not reduced together with the decrease in the polishing time, leading to a surplus of diamond left on the cloth.

In order to finally reach a desired removal rate of ~1–1.3 μm using a combination of 1 μm diamond + OPS polishing, the removal rate by 1 μm diamond should be controlled to ~1 μm/slice or less. If polishing force, polishing time, and dosing period are optimized together (as revealed in the upper-left corner of Fig. 6) a constant removal rate was eventually achieved, as displayed in Fig. 6(b), where the averaged removal rate is measured to be 0.85 μm/slice. Note that this is only the removal obtained by the 1-μm diamond polishing. A further removal is added by the subsequent OPS polishing described in Sec. III C.

Controlling and knowing the removal thickness is challenging. From Figs. 5 and 6, it is concluded that diamond dosing has to be carefully tuned in order to achieve a steady-state suspension density on the cloth: Too little or too much dosing leads to decreasing or increasing removal rate.

C. Chemo-mechanical polishing and its effect on the removal rate

The 1 μm diamond polishing works by mechanical shearing-off of material from the surface. Consequently, the surface is heavily
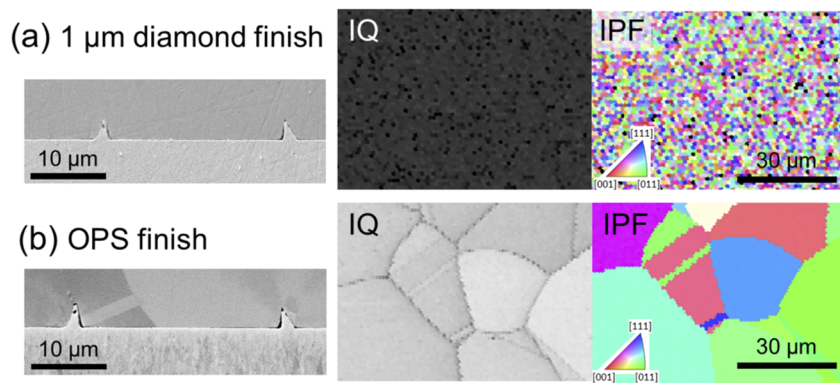

FIG. 7. Comparison of 1 μm finish (a) and OPS finish (b) with regard to EBSD quality. It is noted that the surface quality of (b) was obtained only after 4 min OPS polishing. In both EBSD scans, camera conditions of 4 × 4 binning and 11 ms exposure, with a Hough transform resolution of 120 pixel × 0.5°, were used.

strained and unsuitable for any crystallographic investigation by EBSD or electron channeling contrast imaging (ECCI). As can be seen in Fig. 7(a), even though the scratches appear to be far less than 1 μm in width and depth (~200 nm), the 1 μm diamond finish does not allow to collect EBSD patterns, which stem from the first ~20 nm distance below the surface. Before acceptable EBSD patterns can be obtained, the strained layer has to be removed from the surface. This is achieved by chemo-mechanical polishing using oxide polishing suspension (OPS). Figure 7(b) displays the success to achieve the goal even though the OPS polishing time lasted only 4 min.

OPS functions differently from diamond polishing. Its polishing mechanism is based on a chemical reaction between the polished material and the OPS solution, followed by removal of the product layer by either SiO_2 or Al_2O_3 particles. For example, SiO_2-based OP-S and OP-U have a pH value ~9.5 (alkaline), while Al_2O_3-type OP-A (Struers) is acidic. Different vendors sell OPS products of slightly different particle sizes and compositions, but the general mechanisms of polishing are the same. Throughout the present study, OPS suspension from microdiamant[TM] was used.

Under certain combinations of diamond and OPS polishing a strongly decreasing removal rate was observed, as shown in Fig. 8(a). This observation can be rationalized by the different OPS polishing responses from the metallic sample and the polymeric mounting resin: While the metal is attacked by the OPS suspension, the polymer is immune to it. As indicated by Fig. 8(b), with more and more metal being removed, OPS polishing is less and less effective as the higher resin protects the lower metal from being polished. This effect is also observed on the red curve in Fig. 8(a) that was obtained from OPS polishing alone. The consequence of this selectivity is that OPS polishing must always be complemented by diamond polishing to level out height differences: While the diamond polishing cares for the main removal of both, resin and sample, the OPS polishing is responsible for the creation of a defect-free surface. The latter should anyhow be as short as possible. In our case, the OPS polishing times range between 4 and 6 min. The complete polishing recipe is summarized in Table I.

D. Sample cleaning

Keeping the sample clean throughout the polishing process is a very important issue, first because the sample is eventually investigated under vacuum in a high-resolution SEM, and second because

TABLE I. Polishing recipe employed to obtain, for the current 316 stainless steel, a constant removal rate of 1.1 μm per slice.

Method	Time (min)	Force (N)	Rotation (platen/head) (rpm)	Amount of suspension (mL)
1 μm diamond polishing	1:30	60	155/145	~0.6
OPS polishing	6:00	30	65/55	~8 (50% diluted SiO_2 OPS with demineralized water)

cross-contamination between the different polishing media needs to be avoided. In our system, both the diamond and the OPS polishing procedures are immediately followed by cleaning on different soft cloths to remove the polishing residues; there is no measurable removal of materials from the cleaning.

Before the sample is transferred to the SEM, it needs to be severely cleaned and dried. To this end, the sample is brought to the rinsing station, where the sample is first sprayed at with cleaning liquid from the bottom while the sample carrier rotates. Next, it is dried sufficiently in a flow of compressed air. It is essential to note that no observable droplets should be left on the sample, making sure that the pumping system of the SEM will not be harmed in the long run. Figure 9 summarizes the results of test trials adopting different cleaning media: Among all possible cleaning substances tested (normal tap water, demineralized water, deionized water, and ethanol), demineralized water is chosen to be the most effective; the same figure shows that denatured ethanol, which is usually used to clean samples for SEM observations, results in the worst surfaces. However, the disadvantage of using demineralized water instead of ethanol is that the drying time is longer. Usually, the drying process alone takes in the order of 6 min.

IV. SAMPLE TRANSFER AND POSITIONING

Our system is designed for SEM-based imaging from each serial section. Therefore, the sample is transferred to the SEM after each
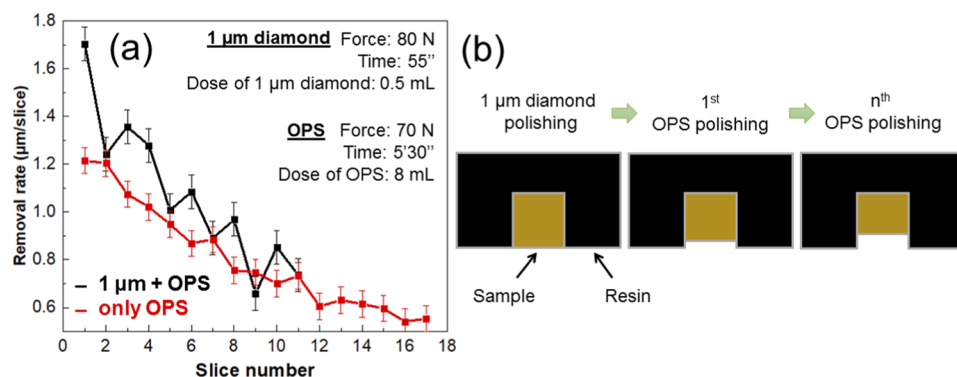

FIG. 8. (a) Effect of combined diamond + OPS polishing (in black) and OPS alone (in red) on the removal rates. The exerted force, the polishing time, and the amount of dosing are shown in the upper right corner. (b) Schematic showing polishing selectivity between the resin and the sample.
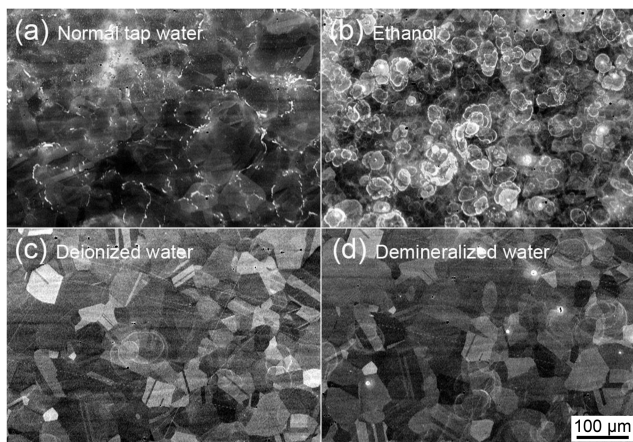
FIG. 9. Different surface qualities with different cleaning substances. (a) Normal tap water and (b) ethanol do not give satisfactory surfaces, while (c) deionized water and (d) demineralized water provide acceptable cleanness. Note that (a-d) are all secondary electron (SE) images.

polishing cycle. The transfer is carried out by the UR5 collaborative robot. After the sample was released from the sample carrier, it is freely standing on the sample transfer bay where it is picked up by the robot. A control whether the sample is picked up correctly is given by both the gripping force and the finger distances. Next, a dedicated script is invoked on the robot to transfer the sample from the recess of the sample transfer bay to an in-house built sample dock at the microscope. This sample dock, displayed in Fig. 10, is designed to allow self-positioning of the sample by means of five spring-supported roller wheels that press the sample against a window frame that keeps the sample surface at a constant height, position, and orientation; the sample "snaps" into the holder once it is released by the gripper fingers. This mechanism allows easy loading and unloading. There is currently no feedback whether the sample insertion has been successful, but, in fact, it has never failed in thousands of trials thus far.
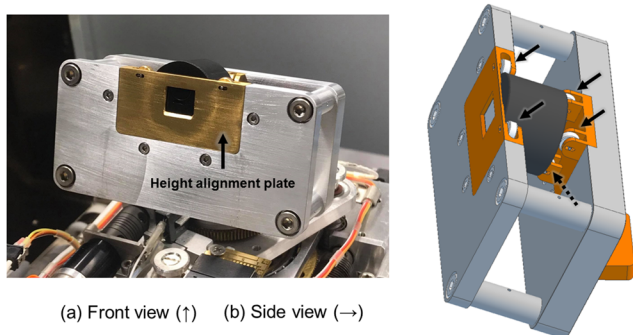

(a) Front view (↑)   (b) Side view (→)

FIG. 10. Appearance of the dedicated 70°-pretilt holder with a polished sample inside. (a) An observation window in the middle of a height alignment plate can be seen from the front view. (b) Five rollers indicated by the black arrows confine the sample position from the side view.

It is noteworthy that the UR5 robot not only places the sample in the holder but also opens the SEM chamber door with its wrist joint, after the chamber has been vented and closes it again after the sample has been inserted into the holder.

The sample dock can take two positions in the microscope: a horizontal sample position for observations by ECCI and a 70° tilted position for EBSD observations. Here, we will only discuss the latter one. Once the chamber door is closed, the microscope is automatically evacuated and high voltage and the electron beam are switched on. Then, an SE image of the markers is taken in order to obtain information on the current slice thickness. Finally, EBSD acquisition is started (with the EBSD camera kept at its position throughout the whole process). For different specimen positions in the chamber, namely, the sample transfer position for the robot, the marker recognition position and the final EBSD acquisition position, different sets of stage x–y coordinates are approached by SEM stage movement. All other axes of the stage are kept at fixed positions. All mentioned processes proceed without any user interference once all positions and imaging parameters have been fixed during the set-up of the measurement. It is, nevertheless, possible to interrupt the process at any time to change parameters, should that become necessary.

The whole transfer process is affected with a certain amount of positional inaccuracy, which is why the exact sample position is never exactly identical for two slices. Detailed discussion regarding this point will be made in Sec. VI A.

V. EBSD DATA ACQUISITION AND RECONSTRUCTION

For the data that were acquired for the present work, EBSD maps were collected through a TSL OIM data collection system with an EDAX Hikari camera. An acceleration voltage of 20 kV, a beam current of about 10 nA, and a working distance of 20 mm were used; dynamic focus was turned on to ensure correct focusing throughout the large scanned area (at a microscope magnification of 100×). For EBSD pattern acquisition from the nearly defect-free, fully recrystallized 316L stainless steel, we used 8×8 binning and 2 ms exposure time to give sufficient EBSD pattern quality. A Hough transform with a $1°$ angular resolution was applied for band detection on 96×96 (pixels) patterns. Under these conditions, the indexing rate could reach up to about 380 fps, almost the upmost that can be reached with the equipment. Being the most time-consuming part of the whole 3D acquisition cycle, EBSD takes around 35 min for mapping an area of $\sim900 \times 900 \ \mu m^2$ size using a rectangular acquisition grid of step size $1 \times 1 \ \mu m^2$. This time corresponds to about 54% of the total cycle time, which is about 65 min. The estimated times spent on the individual steps of a 3D acquisition cycle are illustrated in Fig. 11.

Before 3D reconstruction, each 2D EBSD slice was preprocessed in TSL OIM Analysis 8.5.0. To be more specific, a single-iteration grain dilation algorithm was run to eliminate wrongly indexed pixels at GBs and junctions. All slices were then imported into QUBE,[46] our in-house software for 3D reconstruction and analysis of data. After import, the data were translationally aligned, first manually and then automatically by minimizing the disorientation angles between corresponding voxels for all adjacent slices. Then, the data were cropped, for the present example, to a size of $941 \times 784 \times 24$ (voxels) to remove dangling surface voxels caused
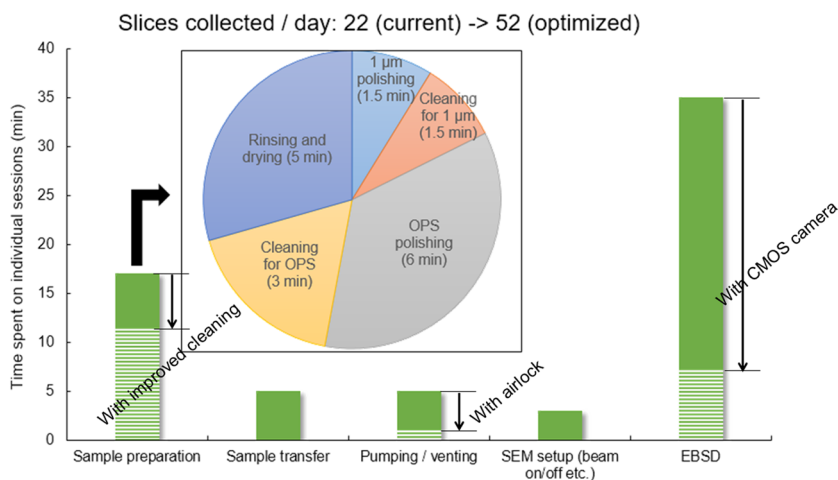
FIG. 11. Detailed description of the time spent in each step in one single slice. In total, one slice of a 900×900 μm^2 sized area (1 μm step size) takes about 65 min cycling time, which can be reduced to 27 min if the cleaning efficiency, pumping rate, and EBSD acquisition speed are optimized (shown in horizontal lines).

by slice registration. An example of a resulting 3D volume is shown in Fig. 12(a). Figures 12(b) and 12(c) demonstrate two perpendicular orthogonal views of the reconstructed volume data: As indicated by the miniframes in the top right corner, Fig. 12(b) is viewed along the X axis, while Fig. 12(c) along the Y axis. Here, the Z-spacing in between the slices was set to 1.1 μm, which is the value obtained from the PFIB marker measurements. In Sec. VI C, this value will be cross-checked based on the results of coherent twin grain boundaries (CTGBs).

Grain reconstruction (segmentation) was carried out with a threshold angle of $5°$; grains with a size smaller than five voxels were ignored. Next, a boundary reconstruction was carried out by discretizing the GBs into a surface mesh of small triangular primitives by applying a marching tetrahedron (MT) algorithm.[46,47] Afterward, in order to eliminate the undesirable mesh roughness and artifacts, GB meshes were smoothed using a surface tension-based method;[48] during this process, the quadruple junctions were pinned, and the number of grains was kept unchanged. After this process, mesh areas in the direct neighborhood of triple junctions were ignored.

In order to plot the five-parameter grain boundary character distribution (GBCD), the aligned and cleaned maps were exported from QUBE and loaded into DREAM.3D.[49] Proper reference frames must be set in the pipelines to get the correct results. The results from DREAM.3D were visualized by the freeware ParaView 5.9.1.[50]

VI. RESULTS AND DISCUSSION

A. System evaluation

The x–y positioning inaccuracy of the sample inside the SEM, as previously mentioned in Sec. IV, results from three different sources: SEM stage movement, SEM chamber opening/closing by the robotic arm, and sample extraction/insertion by the robotic arm, with the last one having the most significant influence. Each individual effect has been tested for 25 cycles. Within 25 cycles, the stage movement causes at maximum 1.5 μm inaccuracy, while the chamber opening/closing is responsible for <10 μm of displacement. Finally, sample extraction/insertion by the robot arm (without involving the polishing process) gives rise to the largest shift of less
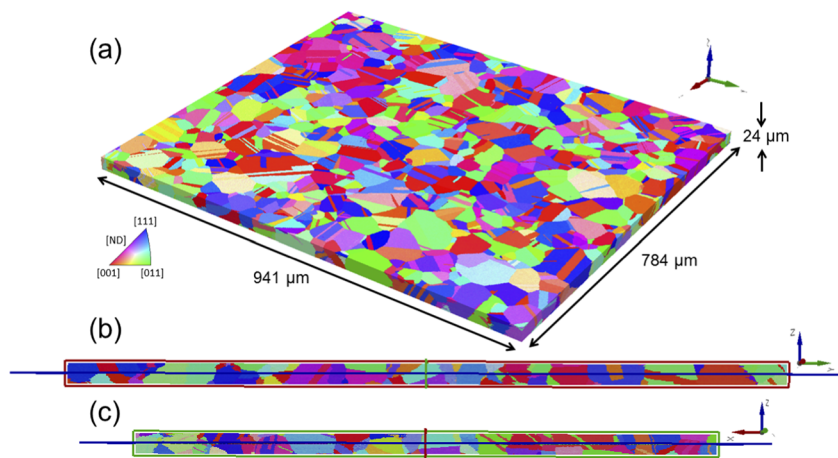

FIG. 12. (a) 3D EBSD stack of a size of $941 \times 784 \times 24$ (voxels). The in-plane square grid has a size of 1×1 μm^2, while the Z-spacing is 1.1 μm. (b) and (c) are two perpendicular views along the X and Y directions, respectively.

than 80 μm. Thus, the overall positioning inaccuracy during the 3D acquisition process is measured so far to be within 100 μm, which is still too high. Currently, this inaccuracy is simply accepted and the data are at the end cropped to fit the common 3D data block. This leads to an undesired loss of ~10% of the data. As an outlook to improve the transfer performance, image recognition will be built in the SEM process followed by an additional stage movement. For this purpose, the non-changing part of the M-shaped markers will serve as references.

Further potential sample positioning errors are sample rotation and sample height. As already mentioned above, the sample rotation is smaller than 0.5° because one of the gripper fingers and the sample have an adjusted geometry that aligns the sample each time it is handled. The sample height is set by a plate that acts as a stop block [see Fig. 10(a)], which is fixed relative to the microscope stage. To our experience, all SE and EBSD images, taken at magnifications up to 1000 times, were always in good focus.

The time spent on individual sections to collect one single EBSD slice is illustrated in Fig. 11. 65 min is estimated for each slice, which means that around 22 slices could be collected per day. Sample preparation takes ~17 min, with about 1/3 of the time used for OPS polishing and more than half dedicated to cleaning. It is recalled here that the ultrasonic bath originally installed in the polishing automaton has been replaced by the sample transfer bay (Fig. 3). Whether ultrasonic cleaning offers a more efficient cleaning in terms of preparation time deserves further exploration. Because pumping the SEM chamber normally takes more than 4 min, an automatic load-lock chamber is definitely an option to increase the throughput.

Currently, EBSD acquisition represents the biggest bottleneck in the entire process cycle. The currently used CCD-based EBSD camera allows a maximum acquisition rate of about 400 patterns per second. With high speed CMOS cameras, this could be speeded up by a factor of 5, provided that our SEM supplies sufficient beam current at an acceptable resolution. Additionally, sparse sampling methods[51] could be adopted, although these are mostly restricted to samples with grains without significant internal orientation gradients.

Employing all the above-mentioned measures for time optimization (see the horizontal-line bars in Fig. 11), the total acquisition time for each slice could be decreased to about 27 min, equaling to around 52 slices collected per day.

B. Advantages and limitations of ELAVO 3D in comparison to other systems

Our ELAVO 3D system stands in competition with a number of other systems that have been designed for the same purpose, i.e., large volume 3D microstructure characterization via EBSD. These systems are Plasma-FIB (PFIB) milling, laser-FIB milling, and broad ion beam (BIB) milling. All these systems have specific advantages and disadvantages, and this chapter will discuss some of the most serious advantages and limitations. The non-destructive x-ray microscopy systems, e.g., the commercially available instruments of XRadia (see, e.g., Refs. 52 and 53), will not be included in the discussion here because they currently still have significantly lower spatial and angular resolution than the EBSD-based systems. Nevertheless, these techniques are of highest interest for materials science as they allow *in situ* observation of samples.

ELAVO 3D can handle, in principle, all samples and materials that can be prepared for EBSD by classical metallographic techniques; this includes soft and hard and many multiphase metallic or intermetallic materials. So far, we have gained experiences with stainless steel (this paper), a martensitic–ferritic dual-phase (DP) steel, different superalloys, 7xxx aluminum alloys, and a beta-titanium alloy. Particularly challenging are multi-phase materials that consist of chemically and/or mechanically very different phases. An example of a successfully prepared multiphase material is a DP steel consisting of a hard and C-rich martensite phase and a soft and C-depleted ferritic phase. Figure 13(a) shows a secondary electron image and an EBSD-based orientation map obtained from the surface prepared by ELAVO 3D. Despite the existence of martensite bands, visible in the orientation map, the surface basically shows no relief. We have not yet explored materials with larger chemo-mechanical contrast, like hard tungsten-carbide crystals in a soft Co-binder material. These are usually prepared for EBSD by a combination of mechanical polishing and Ar^+-beam ion polishing. Such materials are, potentially, inaccessible by ELAVO 3D.

In principle, non-conductive materials, e.g., ceramics or geo-materials, can also be prepared by ELAVO 3D, provided that charging of the sample in the microscope can be prevented, for example, by using a local gas jet in the SEM; here, however, no experience is available yet. Materials that appear so far difficult are those that corrode quickly in aqueous solutions, in particular, Mg and Li alloys, and, for example, certain quickly corroding steels. To the latter belong the Fe–Mn steels, on which we, nevertheless, successfully performed 3D measurements. Figure 13(b) shows one slice of this measurement on a Fe 30 wt. % Mn steel. The surface, in particular along grain boundaries, is attacked by corrosion in the aqueous environment employed for preparation, as visible in Fig. 13(b), but it still gives acceptably good EBSD results. On the other hand, materials that react very slowly under chemo-mechanical etching with OPS may be difficult to prepare, e.g., tungsten or gold, although we have not collected any experience with these materials so far. Problems also appear, so far, on very porous materials, as liquid from the polishing may be preserved in the pores, which then contaminates the surface when applying vacuum.

While the ELAVO 3D system exposes the samples to air and water, all other competing systems keep the samples under vacuum, which is certainly an advantage for the above-mentioned corrosion-sensitive materials.

A further limitation of the ELAVO 3D system appears to be, so far, the minimum layer thickness. Due to the need to combine a mechanical and a chemo-mechanical polishing process, the smallest layer thickness obtained so far is in the order of about 500 nm. Using 250 nm diamond polishing could still reduce this value, but we do not have systematic results available. The BIB technique is claimed to reach, in contrast, layer thicknesses well below 100 nm.[20] The same is true for PFIB technique.[19] The laser-FIB appears to slice thicknesses in the same range as ELAVO 3D.[34]

Another current shortcoming of ELAVO 3D is the scatter of removal thickness, which is in the order of ±10%. It is not clear what exactly the reason is for this. Nevertheless, other techniques achieve better control of the removal, estimated to be in the order of ±5%.
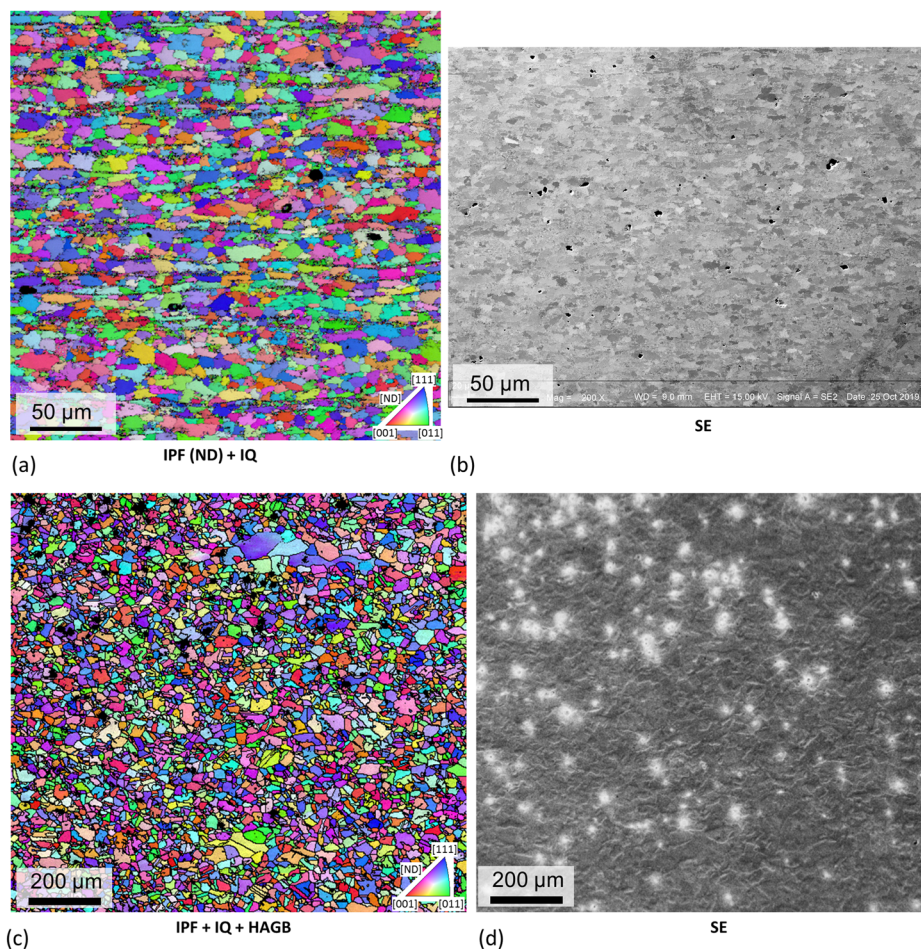
FIG. 13. Examples for successful fully automated preparation of difficult samples. (a) and (b) Dual-phase steel consisting of hard martensite bands in a soft ferrite matrix. (c) and (d) Fe-30 wt. % Mn alloy corroding very quickly in aqueous environment. The figures on the left are EBSD-measured inverse pole figure maps of the map normal direction, and the figures on the right are secondary electron images, taken during the 3D acquisition process.

Currently, we are planning a new design of the QATM polishing robot with the aim to improve the scatter.

A clear advantage of ELAVO 3D compared to all other systems is the perfect planarity of the surface. All other systems create certain weaker or stronger "milling craters" or other surface roughness that may disturb other measurements or imaging techniques (e.g., electron channeling imaging, ECCI, for defect observation or cathodoluminescence for measurement of opto-electronic properties). In addition, curtaining, caused by the presence of differently sputtering material features is a significant problem with all beam techniques. These features can arise from different orientations or different phases that sputter at different rates. Based on our own experience with BIB sputtering and FIB milling, it is clear that curtaining cannot be completely avoided if the material is not perfectly homogeneous. In addition, for the focused beam techniques, curtaining increases with increasing path length of the beam along the surface. This limits the achievable width of the surface in the beam direction. From our own experience,[17] we know that on Ga^+-FIB width is in the order of 50 μm, with PFIB it may be 300–500 μm. For the laser beam, we have no data.

Another advantage is the very large size of the observable non-compromised surface, which is well above all other systems. Of course, it is virtually impossible to map an area as big as a square centimeter by EBSD at high resolution, but the system and the software allow to select any area of interest from such a large surface. In addition, several areas could be mapped in 3D simultaneously or very large x–y–z step sizes (e.g., 10 μm or more) could be used to map large areas.

Finally, it appears that ELAVO 3D currently is the cheapest of all systems. In principle, it requires only a simple SEM (at best, of course, with field emission gun), the transfer robot and the polishing machine as well as the control software. Disregarding the development cost we were able to build this system for significantly less than half of the price of the other systems. It should, however, be mentioned that presently we need access to a PFIB instrument to create the markers. In the near future, however, this will be obsolete as the QATM polishing automaton will have an integrated removal thickness measurement device.

An overview on all systems that have been compared here is given in Table II. It appears that the most powerful instrument so

TABLE II. Comparison of systems for large-volume 3D microstructure observation.[17,19–21,34] The Ga$^+$ system is taken for comparison although it is not a large-volume system. For acronyms, see text.

	Ga$^+$-FIB	Xe$^+$-PFIB	fs-laser FIB	BIB	ELAVO 3D
Removal mechanism	Ga$^+$ ion sputtering	Xe$^+$ ion sputtering	fs laser ablation and Ga$^+$/Xe$^+$ ion	Broad Ar$^{+\,ion}$ beam sputtering sputtering	Chemo-mechanical polishing
Min. removable slice thickness, z(nm)	20	30	500	20	500
Common size of analyzed volume x × y × z (μm^3)	50 × 50 × 50	300 × 300 × 300	1000 × 1000 × 1000	1000 × 1000 × 300	1000 × 1000 × 1000 (potentially bigger)
Removal rate (μm^3/s)	~20 using 65 nA beam[a]	~400 using 65 nA beam	~3500 (laser + PFIB)	~10^5	~>10^4
Estimated removal time per slice (without EBSD)	~15 s for 100 nm	~4 min for 1 μm	~5 min for 1 μm	~10 s for 1 μm	30 min (to be reduced to 22) for 1 μm
Limitations	Very small volume; beam damage; curtaining	Small volume; beam damage; curtaining	Beam damage; curtaining	Curtaining; uneven (concave) area	Corrosion of sensitive samples because of exposure to water and air; inaccuracy of removal rate,
Approximate cost in (Mio $) (without EBSD)	0.8	1.5	1.8	>0.8	0.5

[a]These are values taken from Echlin *et al.*,[34] and our own values would be 0.44 using 500 pA beam to receive EBSD-enabling surfaces.[17]

far developed is the BIB system, though we do not have access to all information on that system. The ELAVO 3D system excels particularly with its large, non-compromised observable area, achievable on many different materials.

C. Coherent twin grain boundaries (CTGBs) as an internal standard to evaluate data reconstruction

316L stainless steel contains numerous (length fraction ~0.54 adopting Brandon criterion[54]) recrystallization twin boundaries owing to its fcc crystal structure with low stacking fault energy. However, in fact, there are by crystallography two types of twin boundaries, i.e., coherent twin grain boundaries (CTGB) and incoherent (ICTGB) ones. CTGBs have strict {111} boundary planes while the ICTGBs do not. The boundary planes can only be known with certainty when they are studied in 3D, but since coherent twin boundaries have special planarity, it is in most cases also possible to distinguish them by a 2D trace analysis.

For 2D analysis, the boundary reconstruction algorithm in TSL OIM Analysis 8.5.0 was applied, taking the trace tolerance to be 2 pixels. The algorithm aims at reconstructing vectorial GB traces from originally pixelated data, where the trace tolerance defines the maximum perpendicular distance between a reconstructed GB and the corresponding pixelated GB. For CTGBs the traces of the reconstructed GBs should then follow the traces of the crystallographic {111} planes as closely as possible.[55] To this end, a tolerance angle, defined as the angular difference between the reconstructed GB trace and the crystallographic {111} trace from each abutting grain, is chosen to be 2°. Finally, a deviation angle ($\Delta\theta$) to the exact twin misorientation relationship also has to be defined, here selected to be 2° as opposed to a more relaxed 8.66° according to the conventional Brandon criterion.[54] It is noted here that the selection of all the threshold values is central but arbitrary. In general, the parameters should be neither too relaxed nor too strict.

Following the reconstruction protocol described in the previous paragraph, Fig. 14(a) shows the grain morphology superimposed with boundaries colored by black (originally pixelated boundaries), yellow (reconstructed vectorial general boundaries), and red (reconstructed CTGBs). If the 2D GBs are all determined to be
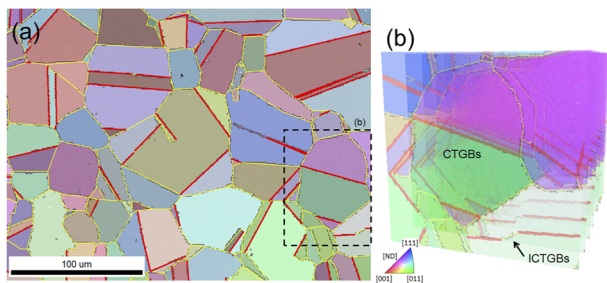
FIG. 14. (a) A two-dimensional EBSD map with the grains color coded by IPF-Z. Reconstructed grain boundaries (GBs) are superimposed, where black GBs are the original, pixelated boundaries, yellow show smooth reconstructed GBs, and red denote coherent twin grain boundary (CTGB) segments. (b) If the 2D CTGB stands true (through trace analysis) throughout the 3D stack, the boundary is finally regarded as a CTGB (in the middle), otherwise as an incoherent twin grain boundary (ICTGB at the bottom right corner).

CTGBs across the 3D stack, the GB is finally regarded as a CTGB [an example is visible in the middle of Fig. 14(b)]. Otherwise, if the GB contains more than one incoherent segment, the GB is not counted as a CTGB [in the bottom right corner of Fig. 14(b)].

Adopting the above-mentioned method, CTGBs in the 3D stack (Fig. 12) were identified, and one CTGB is selected and used as an internal standard to evaluate the quality of the reconstructed data, similar to the approach adopted described in Ref. 56. To be more specific, we discuss the impact of (1) the Z-spacing in between slices and (2) that of the number of repetitions of mesh smoothing cycles.

To study the role of Z-spacing, Z-spacings were varied from 0.8 to 1.4 μm in steps of 0.1 μm for the same CTGB. "L" and "R" sides are used to denote left and right grains with respect to the CTGB. This procedure leads to differently inclined GBs as illustrated in Fig. 15(b). The removal rates measured by PFIB markers are shown in Fig. 15(b), with the averaged value being 1.16 μm. Figure 15(c) displays the contour plots of crystallographic normals of mesh triangles in a stereographic projection in terms of L side and R side [refer to (a)] with different Z-spacings; the width of the normal distribution is mainly due to the mesh smoothing, as will be discussed further below. All normal vectors were averaged and the distance to the closest {111} plane determined. The calculated angular differences are displayed in Fig. 15(d) with colored disks. The indicatively optimum Z-spacing range is marked by green shading. In the same plot, the vertical blue dashed line indicates the average removal rate as obtained from the PFIB markers [Fig. 15(b)]; the blue-shaded region accounts for the standard deviation of the measurements (i.e., ±0.1 μm). Figure 15(e) visualizes both, the volumetric and mesh data adopting a Z-spacing of 1.1 μm. Note that the volumetric data are displayed in an inverse pole figure color code for the sample normal (IPF-Z), while for the smoothly meshed GBs, the color code is the crystallographic IPF color of the mesh normals. For better visualization, this image is available as a 3Dz animation (Multimedia view).

While the marker-method proposes 1.16 μm as average slice distance, the twin method results in 1.1 μm as best fitting distance. The obvious discrepancy between both results motivated us to develop a further method for Z-spacing measurement. This method, as well, is based on the assumption that CTGB are flat and have a {111}-type normal. A plane is fitted to the original voxelated boundary using a least square fitting algorithm. The normal of this plane is calculated in crystal coordinates and its angular distance to the closest {111} plane determined. With this method, a further Z-distance curve was determined for the same boundary as the one above. The resulting curve is plotted into the graph in Fig. 15(d). It displays a sharp minimum at 1.06 μm. At this minimum, the deviation to the true {111} CTGB normal is only 0.36°, similar to that of the meshing method. In contrast, the whole curve resulting from the planar fitting method is systematically shifted by a Z-distance of 0.04 μm from that of the meshing method, a difference that is not yet understood.

There are a number of possible reasons for the relatively large discrepancy between the marker method on the one hand and the mesh and planar fit methods on the other. The most serious problem appears to be a wrong calibration of the PFIB x- and y-measures. Even a slight mis-calibration would lead to deviating angles for the fish bone pattern, which would lead to a systematic error in Z-distance detection. An angular error of about 2.5°, i.e., around 5% of the total angle of 45°, in the side-marker pattern would cause a wrong Z-measurement of 0.1 μm, i.e., ~10%. The marker distances may also be affected by possible drift during milling, or the marker shape might be altered by local straining during hot mounting, both of which will lead to inaccuracies of the subsequent measurements. Furthermore, it is obvious from Fig. 15(b) that, despite the rather stable removal rates, the fluctuations of the curve are still prominent, which will influence the planarity of the final meshed GB. To alleviate this instability, it may be reasonable to reduce the rotation speeds and the exerted force during 1 μm polishing, yet with a penalty of increased polishing time. Finally, a non-uniform map distortion may also lead to local inaccuracies of the GBs, which in turn leads to incorrect mesh normals.

Generally, it is not possible to tell which of the two methods of removal rate estimation is closer to the true value. Nevertheless, in the case where other external means of measuring the removal rate do not exist, CTGBs can be regarded as a good indicator, provided that the Z-spacing is more or less constant across the 3D dataset, which has been the case in the current work.

Note that the data presented in Fig. 15 are obtained from a mesh that had been smoothed by 200 iterations on the raw mesh. The amount of smoothing also plays a role for the results, as displayed in Fig. 16. For a Z-spacing of 1.1 μm the number of smoothing cycles was increased from 50 to 350, in increments of 50. It is clearly seen that the deviation angles decrease very quickly during the first 100 cycles from about 2.5° degree for the raw data to an average of 0.4°. With more cycles, the distances do not change any longer. In contrast, the width of the GB normal distribution, measured as full width at half maximum (FWHM) of the distribution continuous to decrease from a value of almost 18° for 50 cycles to about 8° after values larger than 150 cycles. This indicates that the boundary becomes more and more flat, but never flatter than about ±4°.
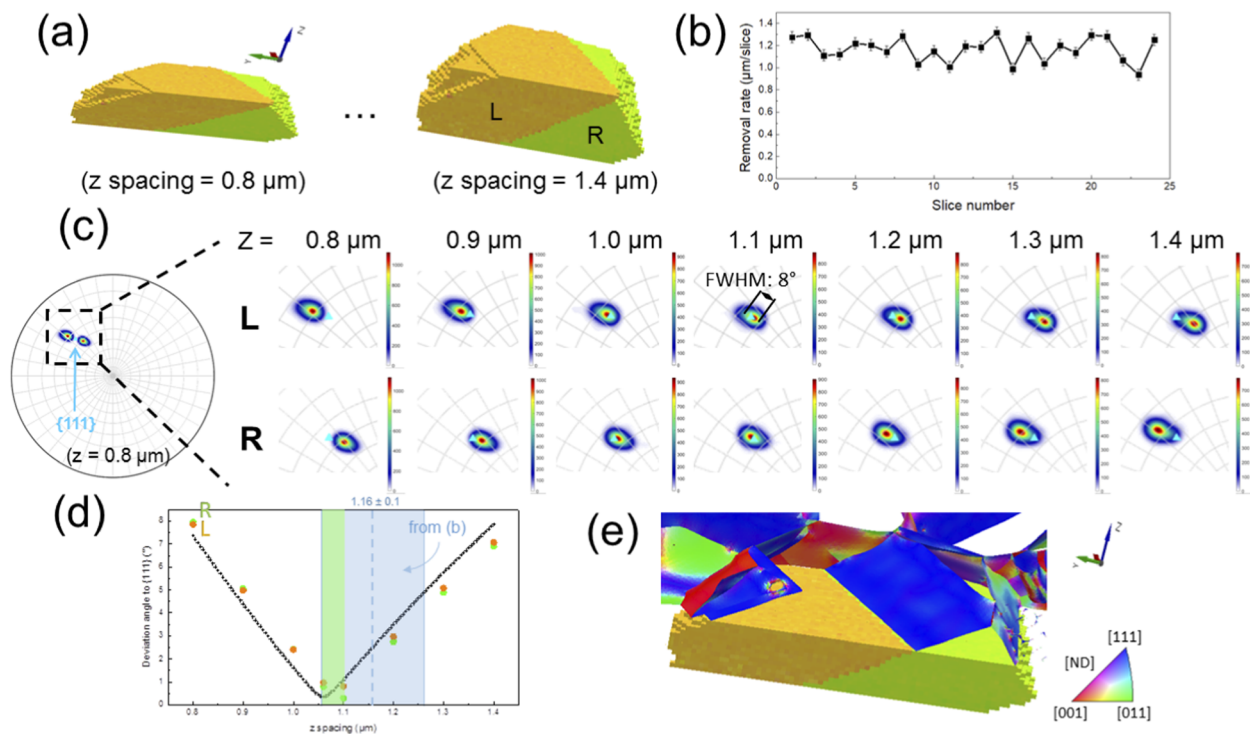
FIG. 15. (a) CTGBs revealed in 3D with different Z-spacings. L and R denote left and right sides of the grain; (b) Removal rates measured by PFIB markers at the side of the sample. (c) Pole figure contour plots of the density of normals of the mesh triangles for the left and right side of the GB as a function of Z-spacing. The closest exact {111} position is displayed by blue triangles. (d) Comparison of removal rates measured by the PFIB markers [data in (b)] (blue line and shaded area) and the data obtained by the CTGB serving as an internal standard [data in (c)] (data points in green and orange, optimum range shown by green shading). (e) Overlay of both volumetric and meshed results adopting a Z-value of 1.1 μm. Color code for the volume data is IPF-Z, and that for the meshed surfaces is mesh normal. This image is also available as a 3D movie. Multimedia view: https://doi.org/10.1063/5.0087945.1

Based on the results presented in Figs. 15 and 16, it is claimed that the angular accuracy of our ELAVO 3D system is on the order of 2.5°, if the raw data and Z-spacings measured from the side markers are used. It can be as good as 0.5° if the Z-spacing description can be optimized. With 150 mesh smoothing cycles the angular resolution, which is the ability of the system to separate the plane normals of two very similar grain boundaries, is in the order of ±4° as obtained from the normal distribution in Fig. 16. These values are, for many materials questions that are supposed to be answered with this technique (e.g., grain boundary character distribution and its correspondence to grain boundary property distributions), largely sufficient. They may, however, not be sufficient for the understanding of properties of individual, discrete boundaries. It is known, for example, that the energy of fcc twin boundaries may vary by a factor of five over just 5° of boundary variation.[57] Another example is the cathodoluminescence signal of twin boundaries in Si, which may vary dramatically for incoherent twin grain boundaries with only slight variations of boundary planes.[58]

This brings up the question whether accuracy and resolution can still be improved. Besides the error sources mentioned above (map distortion and oscillating removal rates), a wrong pattern center calibration could cause some deviation. To check this, a single-crystal silicon calibration sample with grids following ⟨110⟩ crystallographic direction and normal along ⟨001⟩ direction was used for testing. The results showed that, indeed, about 1° inaccuracy of the initial raw data may be explained by a systematic error coming from the setup. Furthermore, the large map size of almost 1 × 1 mm² may cause systematic map distortions that may be removed in the future.

D. Crystallographic and morphological analyses on CSL Σ9 GBs

Significant numbers of Σ3 GBs give rise to an elevated concentration of Σ9 GBs (length fraction ~1% adopting the Brandon criterion[54]) that are formed by mutual interaction of two Σ3 GBs. Σ9 GBs have been experimentally studied in Cu,[59,60] Ni,[56,59,61] Al,[62] and high-Mn steels[63] by means of either stereology[59,60,62] or 3D EBSD via FIB slicing[56,63] or polishing.[61] The general conclusion is that the grain boundary character distribution (GBCD) of Σ9 GBs shows a strong tendency to be pure tilt, that is, the common [110] misorientation axis is within the GB plane. However, the morphologies of individual Σ9 GBs have never been correlated with their GBCD, which could be helpful for understanding the individual Σ9
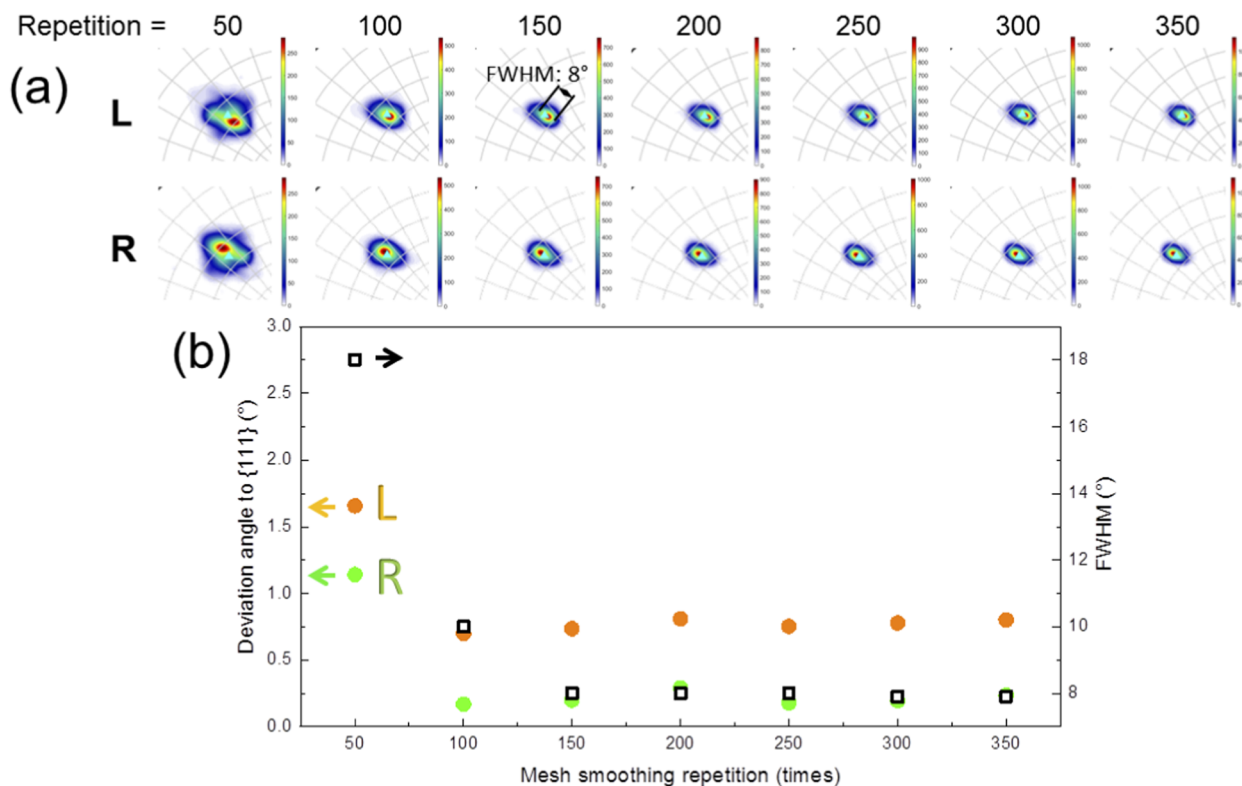
FIG. 16. Effect of mesh smoothing repetitions using the same CTGB as shown in Fig. 15 (for Z-spacing = 1.1 μm). (a) Pole figure contour plots of the density of normals of the mesh triangles for the left and right side of the GB as a function of smoothing repetitions; The closest exact {111} position is displayed by blue triangles. (b) Angular distances between the averaged normals and the closest exact {111} position for each condition displayed by orange and green disk. Full width at half maximum (FWHM) values derived from the normal distributions in the pole figures are displayed as open squares. The FWHM measurement is displayed in (a) for repetition = 150.

characters. Therefore, we present here a detailed analysis of $\Sigma 9$ GBs in terms of both, GBCD and 3D morphology.

To gain statistics, a 3D EBSD dataset of a size of $587 \times 476 \times 72$ (μm^3) was used here. First, Figs. 17(a) and 17(b) show all $\Sigma 9$ GBs highlighted by a 3° deviation angle to that of the exact $\Sigma 9$ misorientation relationship. The terms "inward" and "outward" in Figs. 17(a) and 17(b) mean the GB mesh normals with respect to either one or the other grain of the GB, color-coded according to the inverse pole figure legend, displayed at the bottom left of (b). It is clear at first sight that $\Sigma 9$ GBs do not all show the same pairing of GB normals. In fact, they can be principally categorized into three groups, which are "blue—red" (number fraction = 0.53; area fraction = 0.63), "blue—green" (number fraction = 0.21; area fraction = 0.23), and "red—red" (number fraction = 0.12; area fraction = 0.06). Crystallographically and in the same order, these three color pairs correspond to the following approximately parallel GB planes: {111}‖{115}; {111}‖{110}; {114}‖{114}. Other combinations (number fraction = 0.14; area fraction = 0.08) are either too small or too curved to warrant proper data reconstruction and discussion. Once all the GB mesh normals from all $\Sigma 9$ GBs were joined, they were plotted as grain boundary plane distribution (GBPD), as is shown in Fig. 17(c). Using the same data and taking into

account the tilt-twist characters, the GBCD is plotted [Fig. 17(d)]. Here, the [110] misorientation axis also denotes the two-fold symmetry of the grain ensemble; the same reference frame also holds for Fig. 18. From the GBPD and the GBCD, we observe a clear tendency that the GB planes end up near ($1\bar{1}1$) and (001), with clear tilt character.

A more systematic and detailed overview of the three distinguished cases is displayed in Fig. 18. From left to right in each row, we show both, number (f_N) and area fractions (f_A) of individual cases, their morphologies in 3D for both the original volumetric data and the meshed GBs, the schematic $\Sigma 3$-$\Sigma 3$-$\Sigma 9$ junctions, GBPDs and GBCDs. Case I, {111}‖{115}, is the predominant one, and its morphology features a meeting of a twin variant (T2) with the most densely packed ($1\bar{1}1$) side of another twin variant (T1). For this case, the misorientation then forces the T2 side to be a ($\bar{1}15$) plane, which is verified by both, the GBPD and GBCD that show an asymmetric tilt character. Likewise, case II, {111}‖{110}, also shows an encounter albeit in this case the GB of T1 side is ~ ($1\bar{1}0$), while with respect to T2 there is a sharp ($\bar{1}11$) plane; for the GBCD, the peaks of ($1\bar{1}0$) and ($\bar{1}11$) are also reflected in Fig. 17(d) upon closer examination. Similar to case I, case II is also an asymmetric tilt $\Sigma 9$ GB. Finally, for case III, {114}‖{114}, two
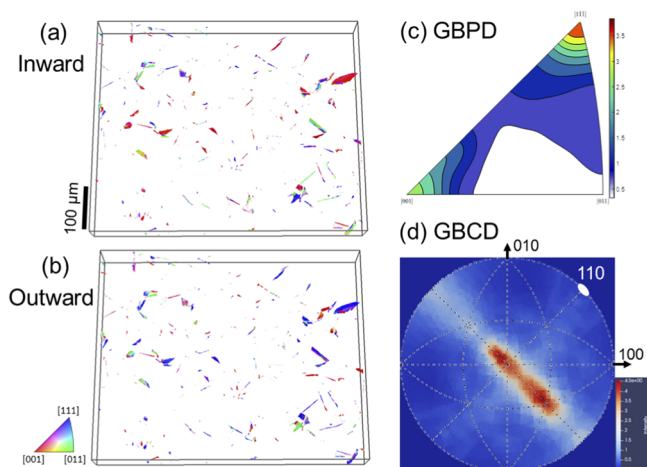
FIG. 17. (a) and (b) All meshed CSL $\Sigma9$ GBs, highlighted by a misorientation deviation of 3° in a 587 × 476 × 72 (μm^3) 3D EBSD dataset. The IPF color coding of the mesh triangles is at the bottom left of (b). (a) shows the normals calculated based on one of the grains of the GB, (b) are the normals with respect to the other one. (c) is the grain boundary plane distribution (GBPD) of all the $\Sigma9$ GBs, and (d) shows the grain boundary character distribution (GBCD). In (d), crystallographic directions [100], [010], and [110] are labeled. [110] is fixed as the misorientation axis.

twin variants join resembling approximately an arrow-shape structure; the GB normals slightly split about the ($1\bar{1}4$) plane, indicating a nearly symmetric tilt character. Since all the GB planes of this kind are found to be very small, it cannot be concluded whether the split is showing their true nature or is due to reconstruction artifacts.

From previous atomistic simulation and experimental studies on $\Sigma9$ GB energies, pure tilt GBs were shown to have lower values compared to other GB characteristics.[56,59,60,63,64] As mentioned above, the ($\bar{1}15$)∥($1\bar{1}1$) asymmetric tilt GBs have with >60% area fraction by far the highest population density of all $\Sigma9$ GB and we assume, therefore, that they have the lowest energy. This was claimed earlier already by Li et al.[56] and Randle et al.[59] In contrast, symmetric tilt {114}∥{114} GBs only make 12% (in number percentage; 6% in area percentage) of the entire $\Sigma9$ GB. Already Rohrer[65] pointed out that a high interface coincidence is not a premise for low energy and high population density. However, it also needs to be mentioned that symmetric tilt {114} GBs were reported in the papers by Ratanaphan et al.[64] and Beladi et al.[63] to have the minimum $\Sigma9$ GB energy. Hence, from literature, there is still a discrepancy of whether symmetric {114} or asymmetric {111}∥{115} result in the lowest GB energy. Furthermore, our observations here show that also {111}∥{110} pairs, which are not discussed in literature, have a significant area fraction.
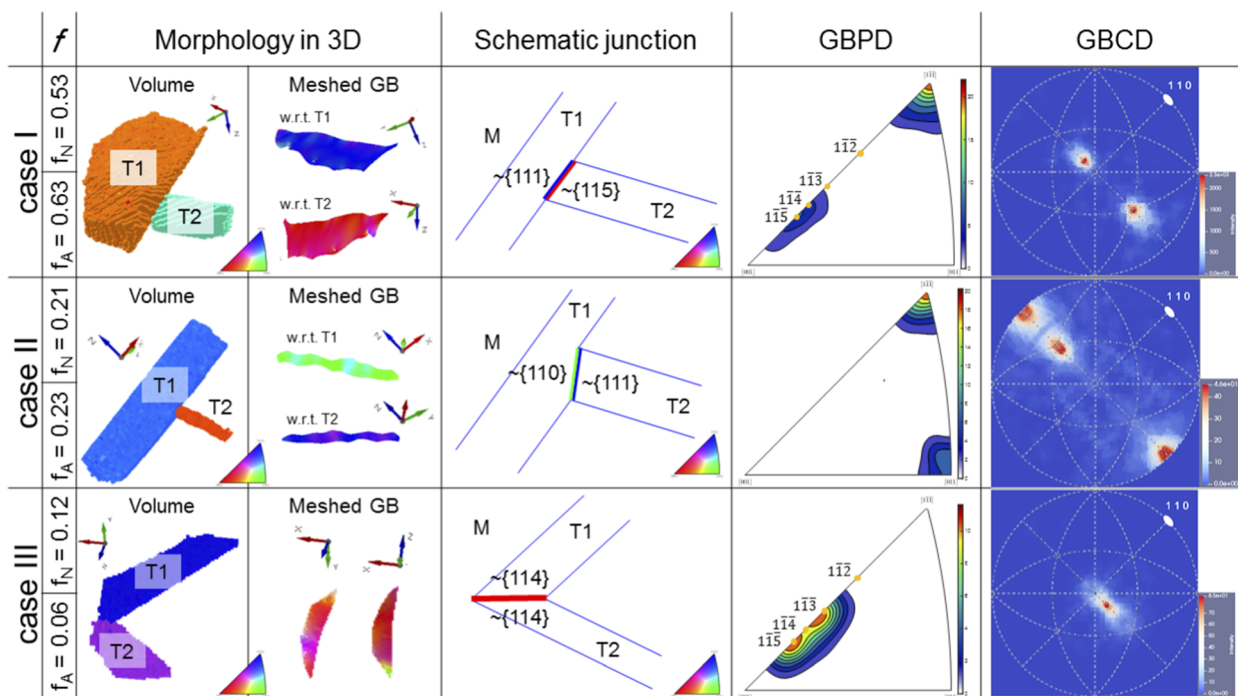

FIG. 18. An overview of three different $\Sigma9$ GB types. From left to right are their fractions (f_N: number fraction; f_A: area fraction), typical morphologies (including volumetric appearances and meshed boundaries) in three dimensions, simplified schematic of their appearances, grain boundary plane distributions (GBPD), and grain boundary character distributions (GBCD). M, T1, and T2 stand for matrix, twin1, and twin2, respectively. The coordinates in GBCD plots are the same as in Fig. 17(d).

The here observed systematic distribution of $\Sigma 9$ grain boundary planes raises the question as to whether the observed GBCD distribution of $\Sigma 9$ GBs is a result of geometrical constraints, of GB energy anisotropy, or of both. The answer to this question turns out to be rather complex as it also needs to take into account the sub-microscopic facet structure of the boundary, which is invisible to the here applied technique. We will, therefore, address this question in a subsequent paper where also electron channeling contrast imaging (ECCI) with a resolution of <10 nm will be invoked to add further structural GB information to the here obtained GBCD.

VII. CONCLUSIONS

An automatic large-volume 3D EBSD system (ELAVO 3D) mainly comprising an SEM (Zeiss crossbeam XB 1540), an adapted polishing automaton (QATM Saphir X-Change), and a collaborative robotic arm (Universal Robots UR5) has been assembled. An in-house designed software talking to an in-house built communication hub controls and reports the whole automation process. The polishing parameters (e.g., polishing time) were thoroughly investigated through a large number of preliminary tests for 1 μm diamond suspension and oxide polishing suspension (OPS). The removal rates were determined by markers, applied to the lateral sample surfaces by a plasma focused ion beam (PFIB), and observed from the polishing surface.

We believe that serial sectioning by mechanical polishing has, compared to other techniques for large-volume sectioning, the greatest potential for the following reasons:

- It delivers very large, perfectly flat and defect free surfaces, also on multi-phase materials.
- The polishing parameters can be adapted to a variety of very different materials. In fact, every material that can be successfully prepared for EBSD by metallographic polishing is accessible (including multi-phase microstructures). The determination of a suitable recipe may require time and efforts, however.
- Removal rates can be set in a wide range and controlled by the selection of polishing parameters.
- The system is mechanically robust and keeps the microscope vacuum in perfectly clean conditions, despite the wet and partly greasy polishing process.

A few numbers illustrate the power of the system:

- Targeted measurable volume: up to $500 \times 500 \times 500$ μm^3 with a 1 μm step size in every dimension.
- Measurement rate: about 30 slices per day with maps of 500×500 pixels.
- Largest measured amount of data points per 3D measurement: around 30.000.000.

3D EBSD datasets with 24 slices, with a total volume of $941 \times 784 \times 24$ (voxels) were reconstructed in which coherent twin grain boundaries (CTGBs) were chosen with the aid of a 2D boundary reconstruction algorithm. The meshed CTGBs in 3D were then used to assess the error of the system in terms of Z-spacing and angular resolution, assuming that the twin boundary normals are exactly {111} planes. In the end, the current automatic system is claimed

to have an angular accuracy of 2.5° for raw data. With appropriate 3D grain boundary mesh smoothing, an angular resolution of ±4° is achieved.

From a much larger volume dataset, the $\Sigma 9$ GB character distribution was investigated. These boundaries show a predominantly tilt character. The boundary plane pairings can be classified into three categories, i.e., $\sim(\bar{1}15)\|\sim(1\bar{1}1)$; $\sim(1\bar{1}0)\|\sim(\bar{1}11)$; and $\sim(1\bar{1}4)\|\sim(1\bar{1}4)$. The first GB pair, an asymmetric tilt boundary, is by far the most frequent, the last, corresponding to a symmetric tilt boundary the least occurring one. Whether geometrical constraints or GB energy anisotropy are responsible for the observed frequency distributions will be investigated in more detail in a subsequent paper.

AUTHOR DECLARATIONS
Conflict of Interest

The authors have no conflicts to disclose.

Author Contributions

Shao-Pu Tsai: Conceptualization (equal); Data curation (equal); Formal analysis (equal); Investigation (lead); Methodology (equal); Visualization (equal); Writing – original draft (equal); Writing – review & editing (equal). **Peter J. Konijnenberg**: Conceptualization (equal); Formal analysis (equal); Methodology (equal); Visualization (equal). **Ivan Gonzalez**: Methodology (equal); Resources (equal); Software (equal). **Samuel Hartke**: Software (lead). **Thomas A. Griffiths**: Conceptualization (equal); Data curation (equal); Investigation (equal); Methodology (equal); Writing – review & editing (equal). **Michael Herbig**: Funding acquisition (supporting); Writing – review & editing (supporting). **Kaori Kawano-Miyata**: Conceptualization (equal); Funding acquisition (equal); Resources (equal); Writing – review & editing (equal). **Akira Taniyama**: Conceptualization (equal); Funding acquisition (equal); Project administration (equal); Writing – review & editing (equal). **Naoyuki Sano**: Project administration (equal); Writing – review & editing (equal). **Stefan Zaefferer**: Conceptualization (lead); Data curation (equal); Formal analysis (equal); Funding acquisition (lead); Investigation (equal); Methodology (equal); Project administration (lead); Writing – original draft (supporting); Writing – review & editing (lead).

DATA AVAILABILITY

All data used and analysed in this article can be obtained on request from the corresponding author, S. Zaefferer, or from the first author, S-P. Tsai.

REFERENCES

[1] K. Schabowicz, Arch. Civil Mech. Eng. **14**, 295 (2014).

[2] N. Duric, P. Littrup, O. Roy, C. Li, S. Schmidt, X. Cheng, and R. Janer, J. Acoust. Soc. Am. **135**, 2155 (2014).

[3] E. Maire and P. J. Withers, Int. Mater. Rev. **59**, 1 (2014).

[4] J.-Y. Buffière, P. Cloetens, W. Ludwig, E. Maire, and L. Salvo, MRS Bull. **33**, 611 (2011).

[5] D. J. Jensen, S. E. Offerman, and J. Sietsma, MRS Bull. **33**, 621 (2011).

[6] W. Ludwig, P. Reischig, A. King, M. Herbig, E. M. Lauridsen, G. Johnson, T. J. Marrow, and J. Y. Buffiere, Rev. Sci. Instrum. **80**, 033905 (2009).

[7] J. Frank, in *Electron Tomography: Methods for Three-Dimensional Visualization of Structures in the Cell*, edited by J. Frank (Springer, New York, NY, 2006).

[8] P. A. Midgley and R. E. Dunin-Borkowski, Nat. Mater. **8**, 271 (2009).

[9] B. Gault, F. Vurpillot, A. Vella, M. Gilbert, A. Menand, D. Blavette, and B. Deconihout, Rev. Sci. Instrum. **77**, 043705 (2006).

[10] T. F. Kelly and M. K. Miller, Rev. Sci. Instrum. **78**, 031101 (2007).

[11] M. Li, S. Ghosh, T. N. Rouns, H. Weiland, O. Richmond, and W. Hunt, Mater. Charact. **41**, 81 (1998).

[12] M. V. Kral and G. Spanos, Acta Mater. **47**, 711 (1999).

[13] T. L. Wolfsdorf, W. H. Bender, and P. W. Voorhees, Acta Mater. **45**, 2279 (1997).

[14] J. Alkemper and P. W. Voorhees, J. Microsc. **201**, 388 (2001).

[15] J. Alkemper and P. W. Voorhees, Acta Mater. **49**, 897 (2001).

[16] M. D. Uchic, M. A. Groeber, D. M. Dimiduk, and J. P. Simmons, Scr. Mater. **55**, 23 (2006).

[17] S. Zaefferer, S. I. Wright, and D. Raabe, Metall. Mater. Trans. A **39**, 374 (2008).

[18] J. Guyon, N. Gey, D. Goran, S. Chalal, and F. Pérez-Willard, Ultramicroscopy **161**, 161 (2016).

[19] T. L. Burnett, R. Kelley, B. Winiarski, L. Contreras, M. Daly, A. Gholinia, M. G. Burke, and P. J. Withers, Ultramicroscopy **161**, 119 (2016).

[20] A. Gholinia, M. E. Curd, E. Bousser, K. Taylor, T. Hosman, S. Coyle, M. H. Shearer, J. Hunt, and P. J. Withers, Ultramicroscopy **214**, 112989 (2020).

[21] M. P. Echlin, M. Straw, S. Randolph, J. Filevich, and T. M. Pollock, Mater. Charact. **100**, 1 (2015).

[22] C. M. Dinnis, A. K. Dahle, and J. A. Taylor, Mater. Sci. Eng.: A **392**, 440 (2005).

[23] J. D. Madison, O. D. Underwood, G. A. Poulter, and E. M. Huffman, Integr. Mater. Manuf. Innovation **6**, 135 (2017).

[24] Y. Adachi, N. Sato, M. Ojima, M. Nakayama, and Y.-T. Wang, in Proceedings of the 1st International Conference on 3D Materials Science (Springer, 2012), pp. 37–42.

[25] O. Forsman, Jernkontorets Ann **102**, 1 (1918).

[26] M. Hillert, "The formation of pearlite," in *Proceedings of Decomposition of Austenite by Diffusional Processes* (Interscience Publishers, New York, NY, 1960), pp. 197–249.

[27] F. N. Rhines, K. R. Craig, and D. A. Rousse, Metall. Mater. Trans. A **7**, 1729 (1976).

[28] F. N. Rhines, K. R. Craig, and R. T. Dehoff, Metall. Trans. **5**, 413 (1974).

[29] D. A. Hull, D. McCammond, D. W. Hoeppner, and W. G. Hellier, Mater. Charact. **26**, 63 (1991).

[30] M. A. Mangan, P. D. Lauren, and G. J. Shiflet, J. Microsc. **188**, 36 (1997).

[31] M. V. Kral, M. A. Mangan, G. Spanos, and R. O. Rosenberg, Mater. Charact. **45**, 17 (2000).

[32] D. J. Rowenhorst, A. Gupta, C. R. Feng, and G. Spanos, Scr. Mater. **55**, 11 (2006).

[33] G. Spanos, D. J. Rowenhorst, A. C. Lewis, and A. B. Geltmacher, MRS Bull. **33**, 597 (2011).

[34] M. P. Echlin, T. L. Burnett, A. T. Polonsky, T. M. Pollock, and P. J. Withers, Curr. Opin. Solid State Mater. Sci. **24**, 100817 (2020).

[35] M. De Graef, M. V. Kral, and M. Hillert, JOM **58**, 25 (2006).

[36] R. T. DeHoff, J. Microsc. **131**, 259 (1983).

[37] J. E. Spowart, H. E. Mullens, and B. T. Puchala, JOM **55**, 35 (2003).

[38] M. D. Uchic, M. A. Groeber, and A. D. Rollett, JOM **63**, 25 (2011).

[39] M. Uchic, M. Groeber, M. Shah, P. Callahan, A. Shiveley, M. Scott, M. Chapman and J. Spowart, *An Automated Multi-Modal Serial Sectioning System for Characterization of Grain-Scale Microstructures in Engineering Materials* (John Wiley & Sons, Chichester, 2012).

[40] L. T. Nguyen and D. J. Rowenhorst, Microsc. Microanal. **23**, 354 (2017).

[41] D. J. Rowenhorst, L. Nguyen, A. D. Murphy-Leonard, and R. W. Fonda, Curr. Opin. Solid State Mater. Sci. **24**, 100819 (2020).

[42] A. Tripathi and S. Zaefferer, Ultramicroscopy **207**, 112828 (2019).

[43] S.-P. Tsai, S. K. Makineni, B. Gault, K. Kawano-Miyata, A. Taniyama, and S. Zaefferer, Acta Mater. **210**, 116822 (2021).

[44] H. Singh and A. M. Gokhale, Mater. Charact. **54**, 21 (2005).

[45] D. An, T. A. Griffiths, P. Konijnenberg, S. Mandal, Z. Wang, and S. Zaefferer, Acta Mater. **156**, 297 (2018).

[46] P. J. Konijnenberg, S. Zaefferer, S. B. Lee, A. D. Rollett, G. S. Rohrer, and D. Raabe, Mater. Sci. Forum **702–703**, 475 (2012).

[47] S. Dillard, J. Bingert, D. Thoma, and B. Hamann, IEEE Trans. Visualization Comput. Graphics **13**, 1528 (2007).

[48] L. A. Barrales Mora, G. Gottstein, and L. S. Shvindlerman, Acta Mater. **56**, 5915 (2008).

[49] M. A. Groeber and M. A. Jackson, Integr. Mater. Manuf. Innovation **3**, 56 (2014).

[50] See http://www.paraview.org/ for information on and download of the publicly available software for 3D graphical data analysis paraview.

[51] V. S. Tong, A. J. Knowles, D. Dye, and T. B. Britton, Mater. Charact. **147**, 271 (2019).

[52] S. Reschka, G. Gerstein, S. Herbst, L. Munk, P. Wriggers, and H. J. Maier, Mater. Lett. **262**, 127177 (2020).

[53] S. A. McDonald, T. L. Burnett, J. Donoghue, N. Gueninchault, H. Bale, C. Holzner, E. M. Lauridsen, and P. J. Withers, Mater. Charact. **172**, 110814 (2021).

[54] D. G. Brandon, Acta Metall. **14**, 1479 (1966).

[55] S. I. Wright and R. J. Larsen, J. Microsc. **205**, 245 (2002).

[56] J. Li, S. J. Dillon, and G. S. Rohrer, Acta Mater. **57**, 4304 (2009).

[57] E. R. Homer, S. Patala, and J. L. Priedeman, Sci. Rep. **5**, 15476 (2015).

[58] A. Stoffers, O. Cojocaru-Mirédin, W. Seifert, S. Zaefferer, S. Riepe, and D. Raabe, Prog. Photovoltaics **23**, 1742 (2015).

[59] V. Randle, G. S. Rohrer, H. M. Miller, M. Coleman, and G. T. Owen, Acta Mater. **56**, 2363 (2008).

[60] S. Ratanaphan, D. Raabe, R. Sarochawikasit, D. L. Olmsted, G. S. Rohrer, and K. N. Tu, J. Mater. Sci. **52**, 4070 (2017).

[61] H. Pirgazi, K. Glowinski, A. Morawiec, and L. A. I. Kestens, J. Appl. Crystallogr. **48**, 1672 (2015).

[62] G. S. Rohrer, X. Liu, J. Liu, A. Darbal, M. N. Kelly, X. Chen, M. A. Berkson, N. T. Nuhfer, K. R. Coffey, and K. Barmak, J. Mater. Sci. **52**, 9819 (2017).

[63] H. Beladi, N. T. Nuhfer, and G. S. Rohrer, Acta Mater. **70**, 281 (2014).

[64] S. Ratanaphan, R. Sarochawikasit, N. Kumanuvong, S. Hayakawa, H. Beladi, G. S. Rohrer, and T. Okita, J. Mater. Sci. **54**, 5570 (2019).

[65] G. S. Rohrer, J. Mater. Sci. **46**, 5881 (2011).